Post-Transcriptional Modular Synthetic Receptors

Xiaowei Zhang[1,4]†, Luis S. Mille-Fragoso[1,4]†, K. Eerik Kaseniit[1,5], Connor C. Call[2], Meng Zhang[2], Yixin Hu[3], Yunxin Xie[2,6], Xiaojing J. Gao[2,4,5]*

[1]Department of Bioengineering, Stanford University; Stanford, 94305, USA.
[2]Department of Chemical Engineering, Stanford University; Stanford, 94305, USA.
[3]Department of Biology, Stanford University; Stanford, 94305, USA.
[4]Sarafan ChEM-H, Stanford University; Stanford, 94305, USA.
[5]Stanford Bio-X, Stanford University; Stanford, 94305, USA.
[6]The Chinese Undergraduate Visiting Research (UGVR) Program; Stanford, 94305, USA.
†These authors contributed equally to this work.

*Corresponding author. Email: xjgao@stanford.edu

Abstract

Inspired by the power of transcriptional synthetic receptors and hoping to complement them to expand the toolbox for cell engineering, we establish LIDAR (Ligand-Induced Dimerization Activating RNA editing), a modular post-transcriptional synthetic receptor platform that harnesses RNA editing by ADAR. LIDAR is compatible with various receptor architectures in different cellular contexts, and enables the sensing of diverse ligands and the production of functional outputs. Furthermore, LIDAR can sense orthogonal signals in the same cell and produce synthetic spatial patterns, potentially enabling the programming of complex multicellular behaviors. Finally, LIDAR is compatible with compact encoding and can be delivered by synthetic mRNA. Thus, LIDAR expands the family of synthetic receptors, holding the promise to empower basic research and therapeutic applications.

Introduction

Cells in multicellular organisms modulate their behaviors in response to cues present in their environment or sent by other cells using endogenous receptors. Therefore, to study and engineer mammalian cells, it is critical to possess the ability to understand and further manipulate such interactions. This capability has been endowed by the development of synthetic receptors, engineered membrane proteins that can be programmed to sense specific inputs and produce customized outputs [1]. Remarkably, synthetic receptors have empowered basic research such as investigating the spatiotemporal dynamics of signaling events [2,3] and neuronal connections [4,5], as well as biomedical applications including but not limited to screening small molecule for drug development [6,7], directing therapeutic cells to ablate anomalous cells [8,9] and building complex multicellular structures for potential tissue engineering [10,11].

Despite the power of synthetic receptors, all modular ones to date rely on transcriptional actuation. We postulate that to expand the applications of synthetic receptors, these could be complemented by using post-transcriptional activation mechanisms, producing synthetic receptors that can be

delivered using either DNA or, uniquely, RNA vectors. For the former, post-transcriptional receptors would synergize with DNA-level controls to improve specificity (e.g., producing a payload based on an tissue-specific enhancer AND the response to a ligand). For the latter, taking advantage of the developments spurred by mRNA vaccines, such receptors could avoid the risk of insertional mutagenesis [12] and enable dynamic dosing. In contrast to DNA vectors, that require nuclear entry, the cytosolic translation of mRNA vectors might also improve the speed, efficiency, and consistency of receptor expression – relevant for cases of transient delivery [13,14]. For both modalities, compatibility with single-transcript encoding would especially accommodate therapeutic scenarios that often face delivery bottlenecks. To use the ablation of anomalous cells as an example, information about both the intracellular state and the surrounding microenvironment would ideally be leveraged simultaneously to identify diseased cells. Existing nucleic acid therapies often only take intracellular cues into account (e.g., elevated signals in oncogenic pathways)–[12], yet such intracellular signals are often highly heterogenous within the tumor[13] and potentially shared with healthy, fast proliferating cells. An mRNA-delivered post-transcriptional synthetic receptor would enable incorporation of microenvironmental cues in addition to or in parallel with the intracellular ones, which would increase the precision of ablation or mitigate the emergence of escaper tumor cells, respectively. In summary, there remains an opportunity for developing modular post-transcriptional synthetic receptors that can expand and complement applications of synthetic receptors.

To design post-transcriptionally actuated receptors, we surveyed different mechanism. The past decades witnessed inspiring examples of post-transcriptional regulators [14–17], yet they rely on endogenous biomolecular complexes, such as the translation initiation complex [14,16] and the exon junction complex that controls mRNA stability [17]. We postulated that the engagement with these complexes subjects the actuation mechanisms to intracellular regulations and that their performance might be sensitive to cellular context [18,19], rendering them difficult to engineer or optimize. Alternatively, we identified RNA editing as a potentially robust post-transcriptional actuation mechanism, as it only requires standalone enzymatic reactions, and small-molecule control of such editing has been previously demonstrated[20,21]. We decided to harness adenosine deaminases acting on RNA (ADAR), an enzyme that edits adenosine (A) to inosine (I), treated as guanosine (G) in translation. Each ADAR consists of a catalytic deaminase domain (e.g., ADAR2dd) and double-strand RNA binding domains (dsRBDs) that recruit it to editing sites [22]. We propose the design of LIDAR (Ligand-Induced Dimerization Activating RNA editing), by replacing the dsRBDs on ADAR2 with domains that recruit ADAR2dd to a synthetic RNA substrate in the presence of a specific ligand (**Fig. 1A**). More specifically, LIDAR consists of three components: two customizable dimerization domains – one fused to an ADAR2dd and the other to a specific RNA binding protein (RBP) – and a reporter RNA molecule harboring multiple RBP recruiting sequences and an in-frame stop codon (UAG) within a double-stranded region as an ADAR substrate. When the reporter RNA is brought into the proximity of ADAR2dd, the stop codon gets edited into a permissive tryptophan codon (UGG), resulting in the translation of the downstream payload.

Here we demonstrate that LIDAR is compatible with a variety of receptor architectures. We show that it is capable of sensing diverse ligands and producing different functional outputs, and is compatible with various cellular contexts. Furthermore, we show that it has the potential to enable the engineering of complex cellular behaviors, such as processing orthogonal inputs in the same cell and spatial patterning based on intercellular communications. Finally, we show that LIDAR

is indeed compatible with compact, single-transcript encoding and, critically, it is possible to deliver a functional LIDAR using mRNA. We expect to further develop this versatile LIDAR platform for post-transcriptional sense-and-response capabilities, expanding the family of synthetic receptors for basic research and therapeutic applications.

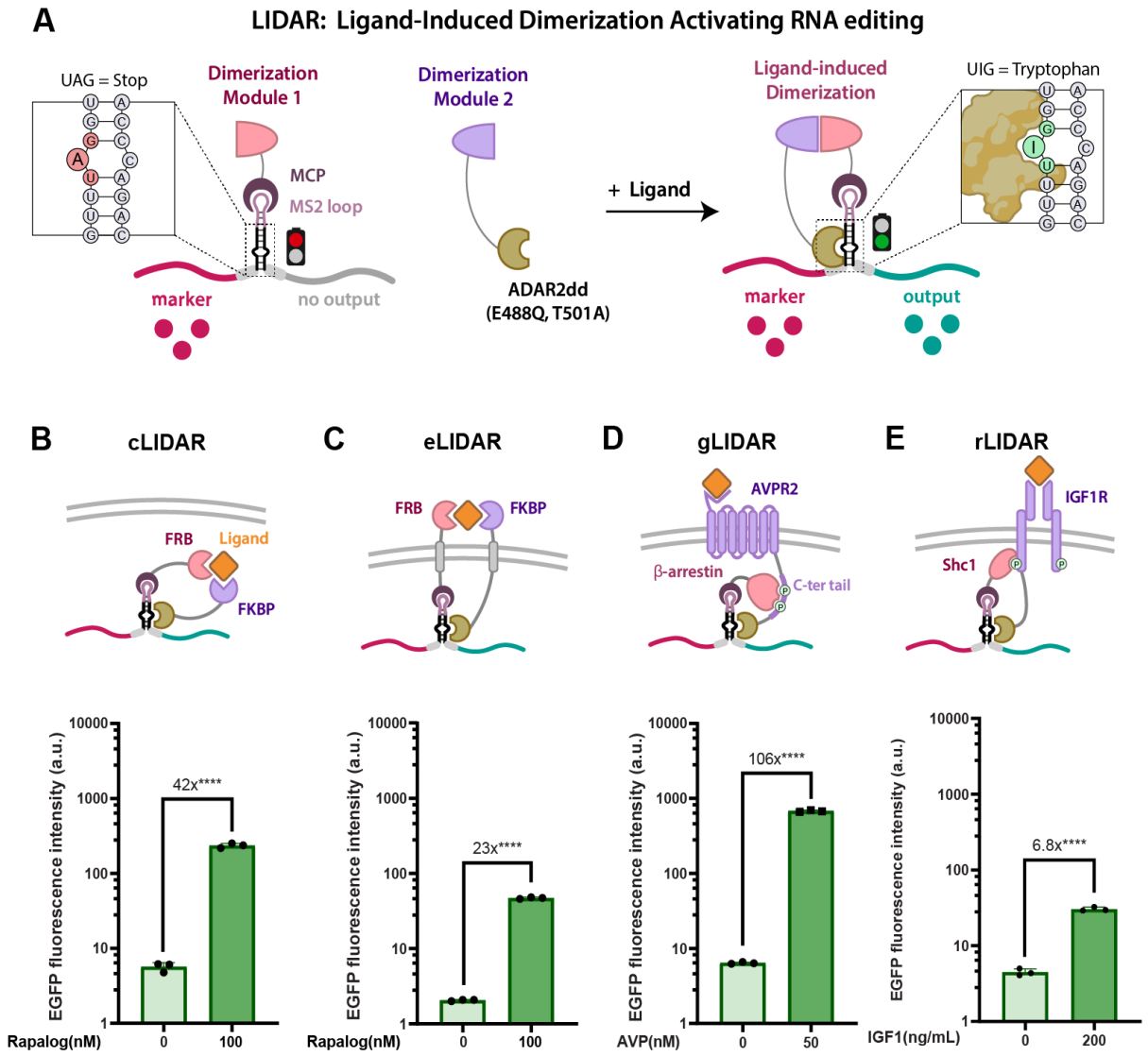

Fig. 1. Design of a modular post-transcriptional synthetic receptor architecture. (**A**) The general LIDAR (Ligand-Induced Dimerization Activating RNA editing) architecture consists of three main components. The first component incorporates a dimerization module fused to an RNA Binding Protein (RBP, i.e., MCP). The second component contains the other dimerization module fused to an ADAR2dd which can edit dsRNAs when in close proximity. The third component is a reporter RNA harboring an in-frame stop codon within a double-stranded stem loop that functions as an ADAR substrate, and multiple RNA stem loops that recruit specific RBPs (e.g., MS2 that recruits MCP). The stem-loop is placed in between the marker and the output, flanked by F2A self-cleavage peptide, preventing translation of the output. The presence of ligand brings the two dimerization modules together such that ADAR2dd comes in proximity to the reporter RNA, triggering editing of the UAG stop codon into a UIG tryptophan codon, leading to payload translation. (**B**) The LIDAR architecture is used to implement a cytosolic binder-based

receptor (cLIDAR), (**C**) an extracellular binder-based receptor (eLIDAR), (**D**) a GPCR-based receptor (gLIDAR), and (**E**) an RTK-based receptor (rLIDAR). The data for each of the implementations represents fluorescent intensities and activation fold-change for induced vs. uninduced conditions. Refer to Methods section for statistical analysis.

Design and optimization of LIDAR

To test the feasibility of LIDAR we started with a system containing FRB and FKBP, two domains that dimerize in response to rapalog (AP21967) [23], to create a cytosolic binder-based LIDAR (cLIDAR). (**Fig. 1B**). To facilitate quantification and iterative engineering, we used a reporter RNA encoding mCherry upstream of the stop codon as the marker and GFP downstream of the stop codon as the output. The stop codon is located in a short dsRNA sequence modified from the endogenous GluR-B R/G site, a canonical ADAR2 substrate [24] (**Supplementary Fig. 1A**), and the reporter RNA includes several MS2 stem-loops to recruit the corresponding phage-derived RBP, MS2 coat protein (MCP) [25]. We then performed optimizations on this initial design. We added the self-cleaving F2A peptides [26] to insulate the marker and the output proteins from the non-functional peptide encoded by the ADAR substrate region. We tested different numbers of tandem MS2 stem-loops (**Supplementary Fig. 1B-C**) [27] and concluded that the output benefits from an increase in MS2 stem-loop repeats. As for ADAR2dd, we hypothesized that the optimal design would possess high catalytic activity, while maintaining low substrate binding affinity to minimize ligand-independent recruitment of the substrate. This motivated us to test two ADAR2dd point mutations: the "hyperactive" mutation E488Q with enhanced catalytic activity, and the "de-dimerization" mutation T501A which might reduce ligand-independent baseline (because dimerized ADAR increase substrate affinity) [28–30], and validated their benefits (**Supplementary Fig. 1D-E**). As a result, our optimal design contains 3 tandem MS2 stem-loops connected to the GluR-B-derived ADAR substrate and adopts both E488Q and T501A point mutations in ADAR2dd, exhibiting minimal leaky baseline and substantial responsiveness to rapalog (**Fig. 1B**).

We then progressed to sense extracellular ligands, while examining the compatibility of LIDAR with a variety of receptor architectures. First, ligand-induced dimerization could be mediated by directly binding to the same ligand on the extracellular side. Inspired by MESA [31], we added a CD28 transmembrane domain between each of the dimerization and actuation modules of cLIDAR (**Fig. 1C**). We validated the response of such an extracellular binder-based LIDAR (eLIDAR) to rapalog (**Fig. 1C**). The response depends on the presence of all LIDAR components (**Supplementary Fig. 1G**). Next, ligand-induced dimerization could also be facilitated indirectly by downstream protein recruitment upon natural receptor activation. Inspired by TANGO [32], we harnessed the recruitment of β-arrestin2 (ARRB2) to the phosphorylated C-terminal tail of a G protein-coupled receptor (GPCR) to create a GPCR-based LIDAR (gLIDAR). Using AVPR2, a GPCR for vasopressin (AVP) previously used in TANGO, we validated an AVP-responsive LIDAR by fusing ADAR2dd to the C-terminal tail of AVPR and MCP to the C-terminus of ARRB2 (**Fig. 1D; Supplementary Fig. 1H-I**). After linker optimization, we determined that short 4 amino acid linkers between LIDAR binding domains and actuation domains results in a low baseline (**Supplementary Fig. 1F**). We demonstrated that gLIDAR can reach activation levels comparable to those of Transcription Factor (TF)-based systems while maintaining a lower baseline (**Supplementary Fig. 1J**), and that these two systems exhibit comparable temporal responses to the ligand (**Supplementary Fig. 1K-L**). Furthermore, to generalize LIDAR to other signaling-induced dimerization events, we demonstrated that LIDAR works with IGF1R, a

receptor tyrosine kinase (RTK), and its activation-dependent binding partner Shc1 (**Fig. 1E**) [32]. Therefore, LIDAR can be implemented using a variety of architectures and can induce robust outputs upon ligand activation.

To maintain a fast design-build-test cycle – unless specified – we performed all our prototyping experiments by transiently co-transfecting receptor-encoding DNA plasmids into human embryonic kidney (HEK) 293 cells. We expect the results to predict LIDAR's ultimate performance in diverse use cases given that we are still testing its mechanism on the mRNA produced from the plasmids.

Compatibility with diverse inputs and cellular contexts

To demonstrate its modularity, we show that LIDAR can sense diverse inputs by employing different architectures. We started by swapping the dimerization domains of eLIDAR for the extracellular domains of IL-2 receptor β and γ, and validated its response to autocrine IL-2 (**Fig. 2A**) while having to yet achieve a reliable response to exogenously administered recombinant IL-2. We then validated that gLIDAR is compatible with several GPCRs, including chemokine receptors CCR6, CCR7 and CX3CR1, as well as the oxytocin receptor (OXT) and β-2 adrenergic (B2AR) receptor (**Fig. 2B; Supplementary Fig. 2A**). It's worth noting that in PRESTO-TANGO [6], an additional V2 tail was included to enhance the signal. For gLIDAR, the additional V2 tail increases both the signal and the baseline, and its effect on fold activation is not always beneficial (**Supplementary Fig. 2A**). For GPCRs like AVPR2 and CX3CR1 that produce a low baseline, the V2 tail improves the fold activation by increasing the activation signal. However, for GPCRs like CCR6 and B2AR that produce higher baselines, the V2 tail also drastically increases the baseline, reducing the fold activation.

To ultimately program more complex multi-cellular behaviors such as cellular homeostasis [33] or directed differentiation [11], as well as to integrate multiple inputs for targeted cell therapies [34], it is often required to have receptors that process orthogonal signals in the same cell. As demonstrated above, gLIDAR is robust and produces strong outputs, making it an ideal candidate for biomedical applications. However, in the current configuration, the ARRB2-RBP fusion protein is recruited to all GPCRs without discrimination. With such design, if we have two gLIDAR receptors in a single cell, the system can only produce one output when triggered by either ligand. We reasoned that, analogous to TANGO vs. ChaCha receptors [35], an inverted version of gLIDAR (orthogonal GPCR-based LIDAR; oLIDAR) can accommodate two or more receptors in a single cell, each producing its corresponding output when activated by the respective ligand. We demonstrated that by fusing ARRB2 to ADAR2dd (ADAR2-ARRB2) and GPCR to an RBP (GPCR-RBP), we can create functional LIDAR receptors (**Supplementary Fig. 2B-C**). Furthermore, using an AVPR2-MCP oLIDAR with a reporter RNA containing MS2 stem-loops (GFP output) and a CX3CR1-PCP (PP7 bacteriophage coat protein) oLIDAR with a reporter RNA containing PP7 stem-loops (mTagBFP output) [36], we showed their orthogonal responses to the respective ligands (**Fig. 2C-D**).

Next, we examined LIDAR's performance in different cellular contexts. To explore the feasibility of the autonomous ablation of diseased cells based on extracellular cues proposed in the introduction, we noted that CCL20 is elevated in some tumor microenvironments [37], and validated rapalog- and CCL20-responsive LIDAR in human colon cancer (Colo 320DM) and

liver cancer (SNU-475) cell lines (**Fig. 2E-F**). As for its potential use in tissue engineering, we validated LIDAR in mouse embryonic fibroblast (C3H) cells (**Fig. 2G**).

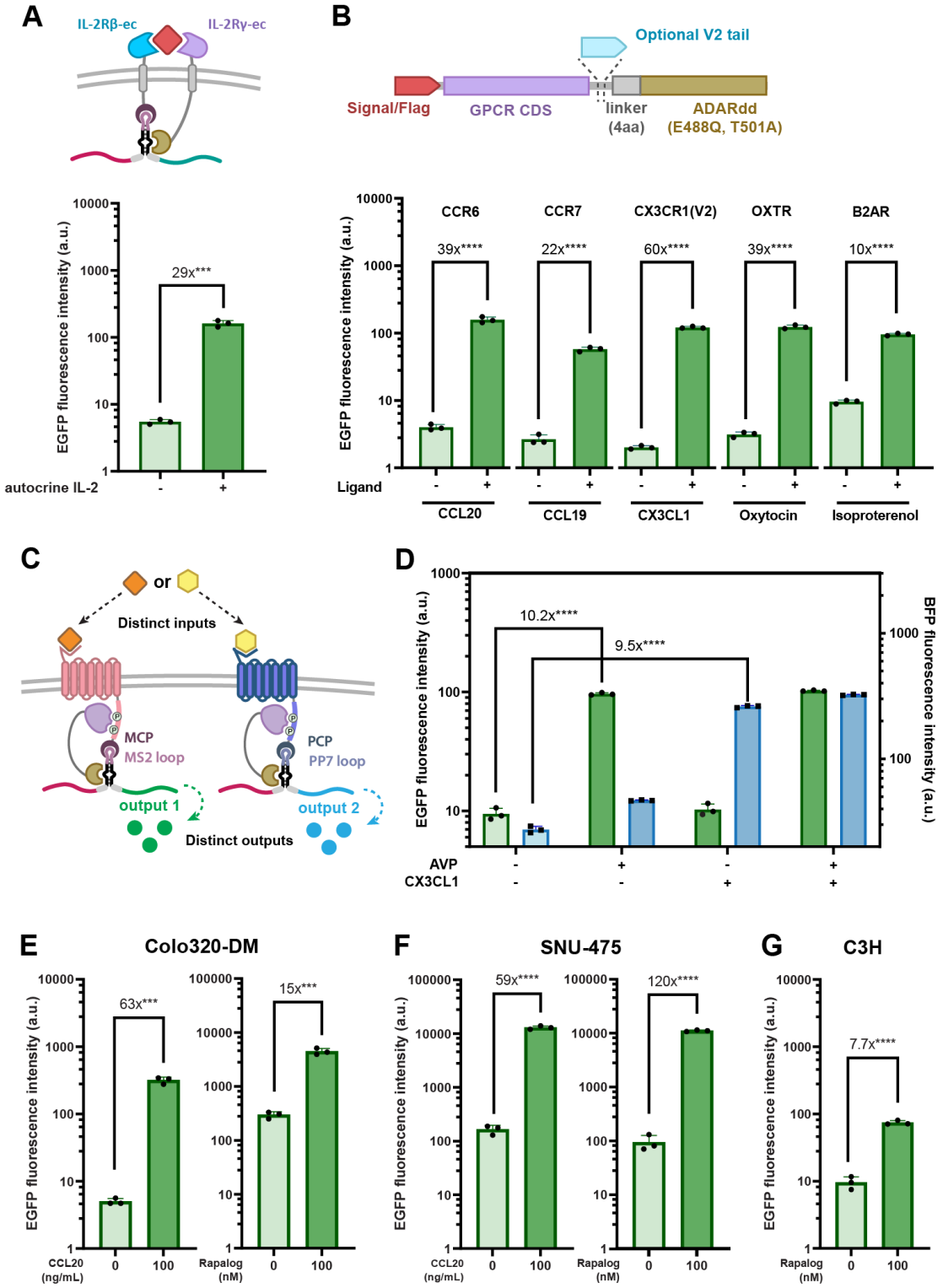

Fig. 2. Molecular and cellular versatility of LIDAR. (**A**) Top panel: Schematics showing the implementation of IL-2 receptor architecture using extracellular binder-based LIDAR (eLIDAR). Lower panel: Data showing the activation of eLIDAR and the production of the output triggered by the presence of IL-2. (**B**) Top panel: Modular design of GPCR-based LIDAR (gLIDAR). Lower panel: Different GPCRs are compatible with the LIDAR architecture with robust signal activation. Refer to **Supplementary Table 3** for ligand catalog and concentrations used. Unless specified, all ligands are applied at the same concentration as listed in Supplementary Table 3. (**C**) Different orthogonal GPCR-based LIDARs (oLIDARs) can be implemented in a single cell to sense different inputs and produce separate outputs. **(D)** Data showing the implementation of both AVPR-based oLIDAR and CX3CR1-based oLIDAR in the same cell. The y-axes for BFP and GFP are in disparate range to portrait both baselines at similar apparent levels while still showing the outputs using their measured values and units, so as to be consistent with other plots in the manuscript. (**E-G**) LIDAR is robust in distinct cellular contexts. LIDAR generates strong activation signal comparable with benchmarking conditions in (**E**) Colon cancer (Colo 320DM) and (**F**) Liver cancer (SNU-475) cell lines with FKBP-FRB eLIDAR and CCR6-based gLIDAR, as well as eLIDAR in **(G)** C3H mouse embryonic fibroblast cell line.

Functional outputs

In addition to fluorescent signals, we tested whether LIDAR output levels are sufficient to produce functional outcomes. We used gLIDAR to produce an iCASP9-based ligand-dependent cell death controller [38] (**Fig. 3A**). We chose iCASP9 as it can efficiently induce apoptosis in response to the dimerizing molecule AP1903[38]. Utilizing a monoclonal HEK cell line (generated by PiggyBac transposon integration; cLSM01) expressing all three components of a CCR6-based gLIDAR and by counting the number of remaining live cells in a well, we demonstrated substantial cell death only in conditions with both the GPCR ligand (CCL20) and AP1903 (**Fig. 3B**). Such quantification based on flow cytometry is consistent with our microscopy-based visual assessments (**Supplementary Fig. 3A**). Notably, we observed no significant killing when AP1903 but not CCL20 is present, suggesting that the low baseline of LIDAR might be adequate for the autonomous ablation paradigm. Additionally, given the broad use of the tobacco etch virus protease (TEVP) [39], we also demonstrated its use as an output to interface with existing protease circuits. We first validated that a LIDAR-produced TEVP rescues a fluorescent protein linked via a TEVP cleavage site to a dihydrofolate reductase (DHFR) degron[40] (**Fig. 3C**). Its dose response curve resembles that of the corresponding LIDAR directly outputting EGFP (**Fig. 3D; Supplementary Fig. 2D-E**). The results not only demonstrate that LIDAR can output functional proteases, but the similarity of the dose-responsiveness curves also indicates that the terminal output of the system is not dampened by the use of the protease. This indicates the potential for LIDAR to be implemented in more complex circuits [41].

Combined with our RELEASE (Retained Endoplasmic Cleavable Secretion) platform [42], the TEVP output can be further used to control the surface display of proteins through the removal of endoplasmic reticulum-retention signals (**Fig. 3C**). Using this strategy, we applied LIDAR's TEVP output to control the membrane display of a human IgG protein [43]. We observed baseline IgG display comparable to the negative control where ADAR2dd is not introduced, and ligand-induced IgG display comparable to a positive control that constitutively expresses TEVP **(Fig. 3E**). The ability of LIDAR to be integrated into RELEASE circuitry is especially useful since we are still optimizing LIDAR to directly output a protein that goes through the secretory pathway (**Supplementary Fig. 3B-C**). Taken together, LIDAR's capability of outputting a membrane

protein not only demonstrates its composability into complex circuits, but also enables intercellular communication essential for key applications we envision.

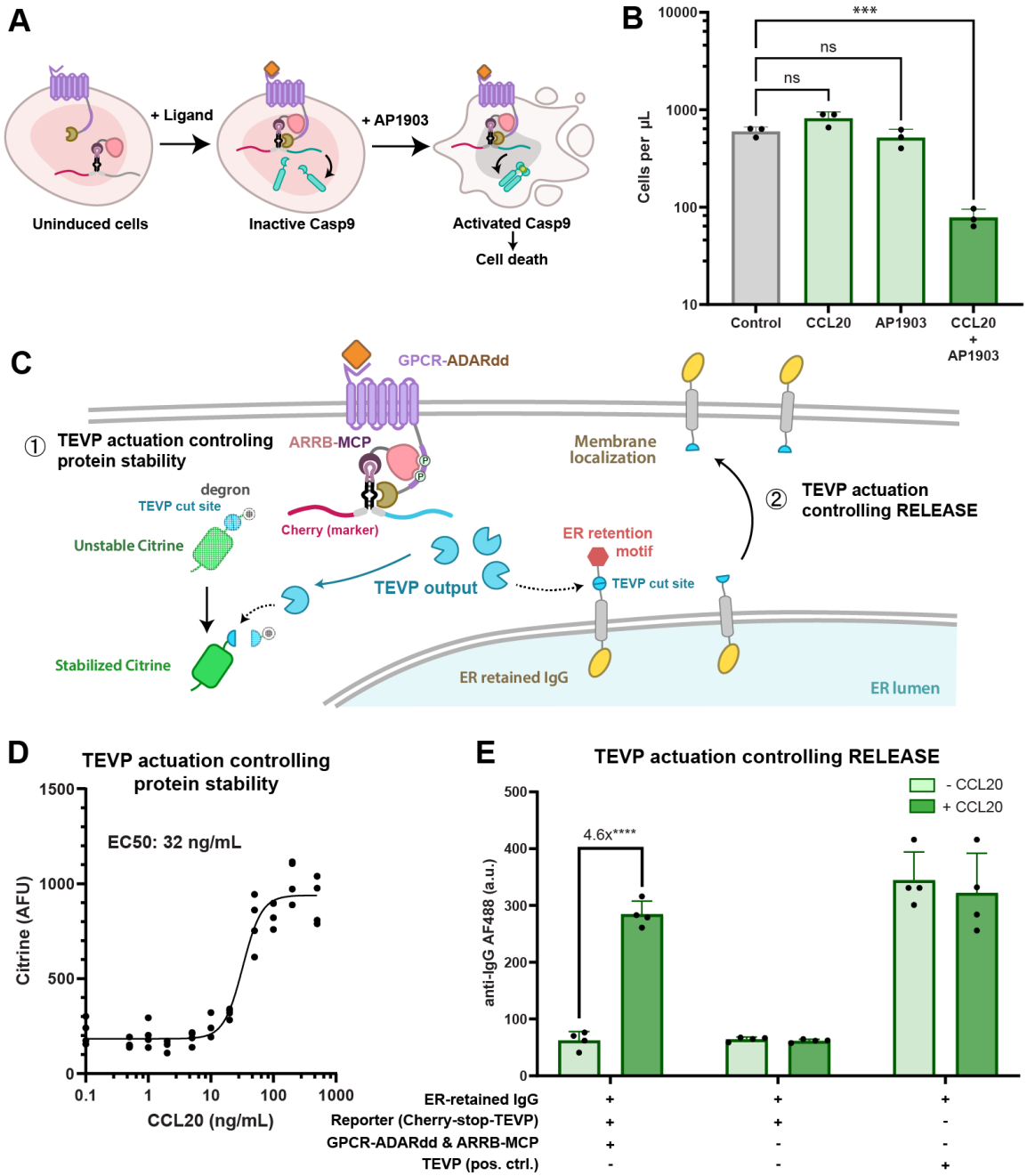

Fig. 3. Expanding LIDAR's output diversity. (**A**) Diagram showing the capacity of LIDAR to drive cell apoptosis by producing a functional iCasp9. (**B**) Quantification of the remaining live cells after LIDAR-induced cell apoptosis. Additional data and information on this assay can be found in **Supplementary Fig. 3A** and the Methods section. (**C**) Schematic demonstrating the versatility of LIDAR and its capacity to interface with existing molecular systems and circuits such as RELEASE [46] and protease-based circuitry [48]. (**D**) Control of protein stability by a protease as LIDAR output. (**E**) LIDAR interface with RELEASE to control the expression of a membrane-bound protein. ER-retained IgG refers to a membrane-bound human

IgG1 retained in the ER by a C-terminal -RXR motif with a flanking TEVP cut site in the middle. IgG1 surface expression levels are measured by staining using a mouse anti-human IgG antibody. Cells are gated on the top 5% of mCherry fluorescence measured by flow cytometry. Refer to the Methods section for a detailed protocol on surface staining.

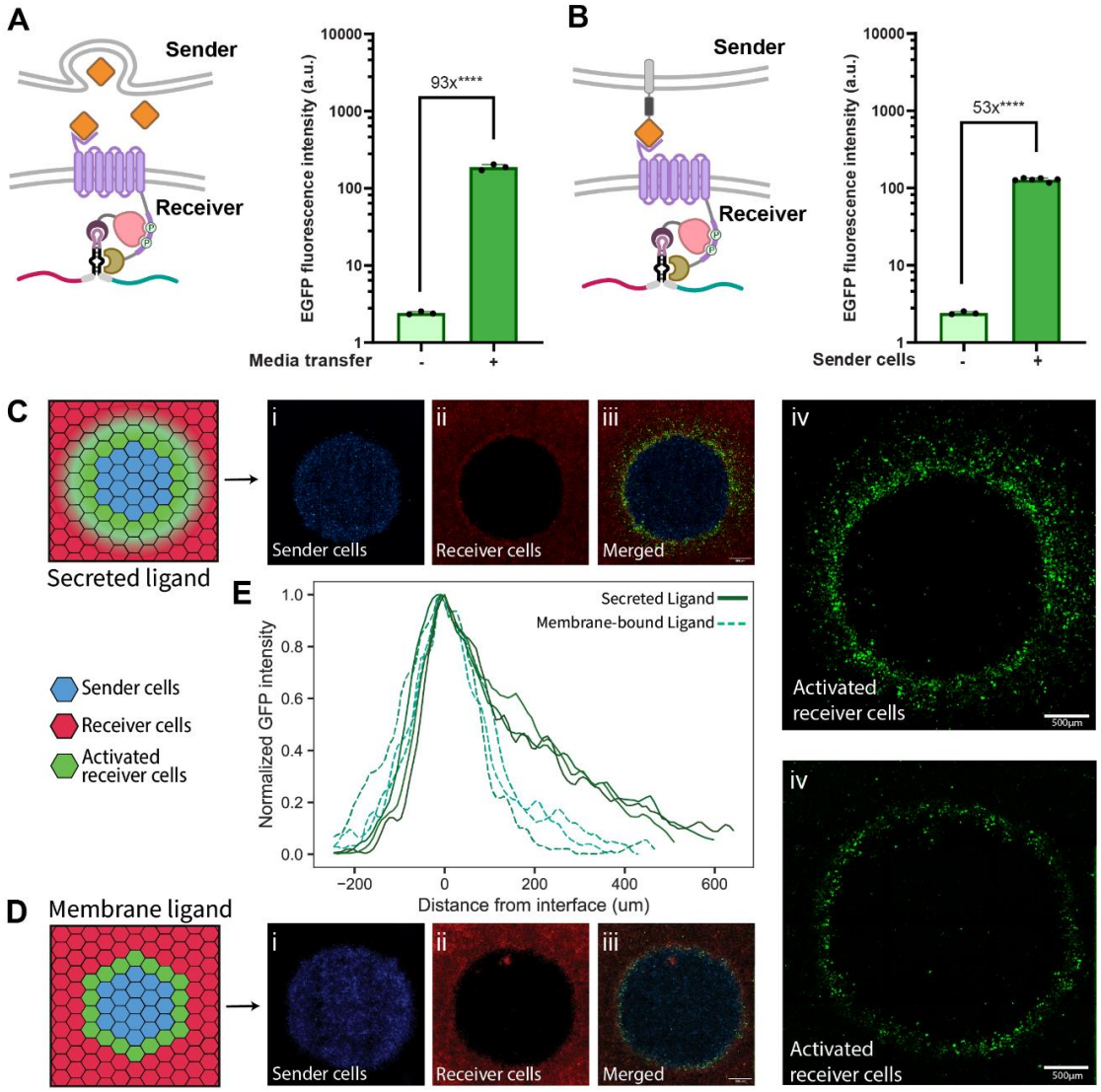

Fig. 4. LIDAR as a tool to drive cell-cell interactions and synthetic patterning. (**A**) Left: LIDAR can detect soluble ligands secreted by other cells. Right: Data showing the response of transiently transfected receiver cells (with CCR6-based gLIDAR) treated with the supernatant from sender cells transiently transfected with soluble CCL20 or WT HEK cells. (**B**) Left: LIDAR is also capable of detecting ligands bound to the membrane of neighboring cells. Right: Data showing the response of transiently transfected receiver cells (with CCR6-based gLIDAR) co-cultured with receiver cells transfected with membrane-bound CCL20 or WT HEK cells. See Methods section for more details and **Supplementary Fig. 4C** for data in stable cell lines. (**C-E**) LIDAR can be used to generate spatial patterns. **(C)** Sender cells producing secreted CCL20 (monoclonal cLSM03) were co-cultured with receiver cells (monoclonal cLSM01) in a circular pattern to demonstrate LIDAR's sensing capabilities and sensitivity. This setup produces a gradient of CCL20 from the center of the circular pattern outwards. The left diagram shows the experimental setup. Images of seeded sender cells (**Ci**), receiver cells (**Cii**), all the channels merged (**Ciii**), and the activated receiver cells (**Civ**) are shown on the right. (**D**) Sender cells producing membrane-bound CCL20 (XZcp07)

were co-cultured with receiver cells (cLSM01) in a similar fashion as in **C**. Individual panels are the same as for the secreted ligand condition (**Di-iv**). For a membrane-bound ligand, we see a thinner and circular pattern more constrained to the sender-receiver interface. The overall GFP intensity is lower compared to the soluble ligand condition due to weaker activation as shown in **Supplementary Fig. 4C**. (**E**) Concentric intensity profiles for both secreted and membrane-bound conditions. Average intensity values were measured. A graphical demonstration of how these average values is calculated can be found in **Supplementary Fig. 4D**. Each condition was measured in triplicates. Refer to the Methods section for more information on the seeding and co-culture process, image acquisition, and processing and quantification of the intensity profiles. A nonlinear background subtraction, as well as a linear enhancement of the brightness and contrast to aid with visualization were performed on all images as detailed in the Methods section.

Synthetic spatial patterning

Inspired by examples from synNotch [10,11,44] and given the advantage that LIDAR could potentially sense both membrane-bound and soluble ligands, we next asked whether we could use LIDAR for synthetic spatial patterning, as a prelude to programming complex multicellular behaviors [10,11,45]. We first validated that CCR6-based LIDAR indeed senses its ligand, CCL20, when the receiver cells are either exposed to conditioned media from CCL20-secreting cells (**Fig. 4A**) or co-cultured with cells displaying CCL20 on their surface (**Fig. 4B**) [46]. We tested whether such contact-dependent and soluble ligand sensing features of LIDAR could be used to program distinct spatial patterns as a preliminary demonstration of spatial programming [44]. When we plated receiver cells (monoclonal cLSM01 with stable integration of CCR6-based LIDAR) surrounding sender cells that secrete CCL20 (monoclonal cLSM03; **Supplementary Fig. 4A**), we observed a response gradient going from the sender cells outwards **(Fig. 4C; Supplementary Fig. 4B**). In contrast, when we tested receiver cells with sender cells producing membrane-bound CCL20 (monoclonal XZcp07), the response pattern is limited to the sender-receiver interface (**Fig. 4D; Supplementary Fig. 4B**). Activated cells far from the direct interface between the two populations are a product of the seeding process and, in particular for the membrane-bound ligand condition, cell migration causing an overlap between the two population produces a band of activated cells. We noted different output intensities produced by the membrane-bound and secreted ligand conditions (**Supplementary Fig. 4C**), presumably due to the different amounts of available ligand per receiver cell given the spatial differences of direct cell-cell contact vs. soluble ligand. We computationally normalized the receiver signals to their respective peak values and extracted LIDAR's output intensity profiles in response to membrane-bound and secreted ligands (**Supplementary Fig. 4D**). As expected, the responses to secreted ligands exhibit longer tails (**Fig. 4E)** than those to the membrane-bound ligands. These results indicate the feasibility of using LIDAR for juxtracrine and paracrine spatial patterning.

Unique delivery features

Lastly, we aimed to demonstrate the unique delivery features enabled by LIDAR's post-transcriptional nature. As many applications are limited by a delivery bottleneck, a post-transcriptional design could enable the compact encoding of all components. It would increase delivery efficiency by reducing the number of vectors needed and improve performance robustness by "locking in" optimal stoichiometry. We encoded all LIDAR components on a single transcript by separating the components with encephalomyocarditis virus (EMCV) internal ribosome entry sites (IRES) (**Fig. 5A**), and indeed observed LIDAR performance comparable to the corresponding

multi-transcript version (**Fig. 5B**, compared to **Fig. 1D**). Second, given our initial motivation of compatibility with RNA delivery, we tested whether LIDAR is still functional when encoded and delivered purely by mRNAs transcribed *in vitro*. We *in vitro* transcribed (IVT) all three LIDAR components into individual mRNAs. The mRNAs encoding the two protein components (CCR6-ADARdd and ARRB2-MCP) were synthesized with 100% of uridine substituted by N^1-methylpseudouridine ($m^1\Psi$) to enhance translational capacity as well as biological stability, and reduce immunogenicity [47,48]. Since base modifications are known to affect stop codon recognition [49], and might potentially affect ADAR editing, we synthesized the LIDAR reporter mRNA with a combination of different percentages of two base modifications commonly used in synthetic mRNA, $m^1\Psi$ and 5-methylcytosine (m^5C), to explore the best-performing combination in our system [50,51]. We observed a significant increase in the EGFP output in response to the ligand (**Fig. 5D**) when co-transfecting with a LIDAR reporter mRNA without base modifications. Although we observed that incorporating base modifications lead to an increase in marker expression (**Supplementary Fig. 5B**), these base modifications also resulted in a decrease in the fold activation of the output (**Supplementary Fig. 5A**). These observations are potentially caused by base modifications affecting baseline editing, stop codon skipping, interference with ADAR binding and catalytic activity, or mechanisms yet to be revealed, indicating the complex role of base modifications in regulating biological activities on synthetic mRNAs. We note that our best fold activation with mRNA transfection (**Fig. 5D**) is about 4-fold lower than the DNA-encoded version (**Fig. 2B**), which is most likely due to the transient nature of mRNA, suggesting the need for further mRNA-specific optimizations to enhance output production. Taken together, our data shows that LIDAR can indeed be delivered purely by mRNA, which opens up new opportunities for RNA-empowered synthetic biology and therapies.

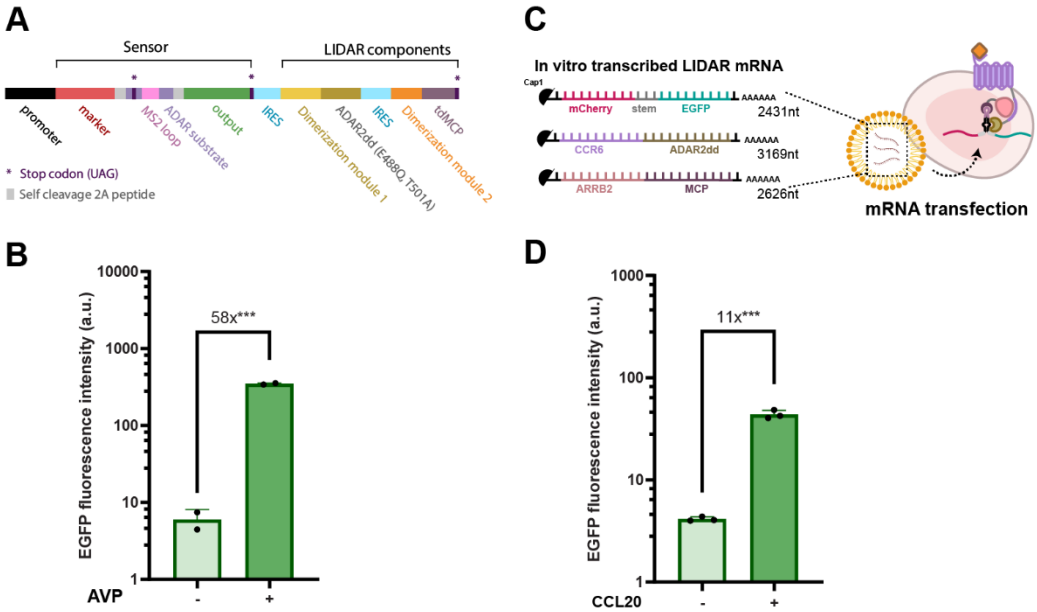

Fig. 5. LIDAR can be encoded as a single transcript and is RNA-compatible. (**A**) Schematics of the single transcript encoding of LIDAR. (**B**) Data showing EGFP output activation by transient transfection of a single transcript-encoded AVPR2-based gLIDAR. (**C**) Experimental setup of an RNA-delivered CCR6-based gLIDAR. Each LIDAR component was delivered as an individual mRNA strand. (**D**) Data showing EGFP output activation by mRNA-delivered LIDAR system regarding the setup in (C). mRNA transfection was performed using 500 ng of each LIDAR component mRNA. The reporter mRNA was

synthesized without base modifications, while mRNAs of CCR6-ADAR2dd and ARRB2-MCP were synthesized with 100% N1-methyl-pseudouridine substitution.

Discussion

In this work, we present LIDAR, a novel design for building post-transcriptional synthetic receptors. The use of standalone ADAR editing as an actuation mechanism enabled hypothesis-driven, iterative engineering (**Supplementary Fig. 1D-E**) and resulted in a modular receptor platform compatible with various receptor architectures (**Fig. 1, 2**), output types (**Fig. 3**), and cellular contexts (**Fig. 2E-G**). These characteristics, combined with compact encoding and potential delivery by mRNA (**Fig. 5**), could eventually enable broad applications in basic research and biomedicine.

Standing on the shoulders of previous modular synthetic receptors, LIDAR both inherits some of their features and offers unique benefits. The modularity of LIDAR enabled us to tap into the rich history of receptor engineering, and created functionally RNA-compatible versions of MESA [31], Cha-Cha [35], and TANGO [32]. In our preliminary comparison (**Supplementary Fig. 1J**), we appeared to have achieved an almost negligible baseline, even when a large amount of LIDAR is introduced through plasmid transfection, while maintaining a ligand-induced signal comparable to a transcription-based synthetic receptor. Given the (often non-linear) amplifications in transcriptional synthetic receptors, they need to be carefully dosed or engineered to mitigate runaway baselines [52,53] as we learned through our own experiences and personal communications. We postulate that LIDAR might have mitigated the baseline issue based on its more limited degree of amplification, although further comparisons will be required to determine that in more contexts. Meanwhile, although **Fig. 3** indicates that LIDAR can output sufficient levels of proteins to alter cellular phenotypes, there might be scenarios where stronger outputs are needed and transcriptional receptors become the preferred choice. Although the most unique feature of LIDAR is its RNA compatibility, these more nuanced comparisons are worth considering when choosing the proper receptor for a specific application.

Further optimizations of LIDAR are required to prepare it for the envisioned applications. First, on the functionality front, because it bypasses transcription, LIDAR could potentially exhibit a faster response than transcription-based synthetic receptors, which we have yet to achieve. We will systematically identify the rate-limiting steps in LIDAR operation and optimize to speed up its kinetics. Second, although we can already indirectly output membrane proteins using RELEASE, we will analyze the mechanism underlying LIDAR's current inability to directly output secretory proteins and fix it accordingly to streamline the design. On the delivery front, first, although we have achieved compact encoding by DNA, compact encoding on IVT mRNA has remained challenging potentially due to decreased efficiency in mRNA synthesis and mRNA stability with longer transcript [54–56]. Such single-RNA encoding would help ensure the optimal stoichiometry of LIDAR components. We envision that this could be solved by advances in IVT protocols [54], incorporation of stabilizing elements on mRNA [56], and optimizing IRES to enable stronger translational [57]. Second, as complete substitution using pseudouridine appears to abolish LIDAR functionality, we will explore alternative RNA synthesis protocols, such as first synthesizing the stem-loop region using regular uridine, and then using splint ligation to connect it to the rest of the reporter RNA harboring pseudouridine [58]. Finally, the off-target editing caused by ADAR2dd still needs to be analyzed at the transcriptomic level.

The current iteration of LIDAR already offers useful tools, and, pending future improvements, it has the potential to empower even more applications in both basic research and biomedicine. The rapalog-responsive LIDAR could be readily applied as a post-transcriptional inducible system, either on its own for scenarios where transcriptional control is unfeasible (e.g., delivery using an RNA viral vector), or in synergy with transcriptional control to improve specificity or signal-to-noise ratio. For basic research, LIDAR could be used to visualize or manipulate specific neurons based on their exposure to endogenous neurotransmitters or connection with other neurons. More importantly, if we overcome the technical challenges associated with mRNA encoding and delivery, LIDAR might offer unique capabilities to next-generation therapeutics. First, similar to the use of SynNotch to modulate the efficiency and specificity of *ex vivo* engineered CAR T cells [59–61], LIDAR would be able to regulate *in vivo* CAR T cells generated by mRNA delivery. Second, we will more thoroughly and rigorously test LIDAR in cancers, so that one day it could be applied to precisely deliver cargos in cancer cells to ablate the tumor and engage the immune system. Beyond removing anomalous cells, LIDAR could also help create beneficial cell types or tissues by processing and guiding spatial cues, again using mRNA to transiently modify endogenous cells without the need for cell extraction and transplantation. Taken together, we are hopeful that future iterations of LIDAR will inhabit an opportune position at the junction between RNA medicine and synthetic biology.

References

1. Manhas, J., Edelstein, H. I., Leonard, J. N. & Morsut, L. The evolution of synthetic receptor systems. *Nat. Chem. Biol.* **18**, 244–255 (2022).
2. Lee, D. *et al.* Temporally precise labeling and control of neuromodulatory circuits in the mammalian brain. *Nat. Methods* **14**, 495–503 (2017).
3. Kim, M. W. *et al.* Time-gated detection of protein-protein interactions with transcriptional readout. *eLife* **6**, (2017).
4. Huang, T.-H. *et al.* Tracing neuronal circuits in transgenic animals by transneuronal control of transcription (TRACT). *eLife* **6**, (2017).
5. Talay, M. *et al.* Transsynaptic Mapping of Second-Order Taste Neurons in Flies by trans-Tango. *Neuron* **96**, 783-795.e4 (2017).
6. Kroeze, W. K. *et al.* PRESTO-Tango as an open-source resource for interrogation of the druggable human GPCRome. *Nat. Struct. Mol. Biol.* **22**, 362–369 (2015).
7. Chen, H. *et al.* Highly multiplexed bioactivity screening reveals human and microbiota metabolome-GPCRome interactions. *Cell* **186**, 3095-3110.e19 (2023).
8. Roybal, K. T. *et al.* Engineering T Cells with Customized Therapeutic Response Programs Using Synthetic Notch Receptors. *Cell* **167**, 419-432.e16 (2016).
9. Hong, M., Clubb, J. D. & Chen, Y. Y. Engineering CAR-T Cells for Next-Generation Cancer Therapy. *Cancer Cell* **38**, 473–488 (2020).
10. Toda, S., Blauch, L. R., Tang, S. K. Y., Morsut, L. & Lim, W. A. Programming self-organizing multicellular structures with synthetic cell-cell signaling. *Science* **361**, 156–162 (2018).
11. Garibyan, M. *et al.* Engineering Programmable Material-To-Cell Pathways Via Synthetic Notch Receptors To Spatially Control Cellular Phenotypes In Multi-Cellular Constructs. *BioRxiv* (2023) doi:10.1101/2023.05.19.541497.
12. Wu, M.-R., Jusiak, B. & Lu, T. K. Engineering advanced cancer therapies with synthetic biology. *Nat. Rev. Cancer* **19**, 187–195 (2019).
13. Dagogo-Jack, I. & Shaw, A. T. Tumour heterogeneity and resistance to cancer therapies. *Nat. Rev. Clin. Oncol.* **15**, 81–94 (2018).
14. De Gregorio, E., Baron, J., Preiss, T. & Hentze, M. W. Tethered-function analysis reveals that elF4E can recruit ribosomes independent of its binding to the cap structure. *RNA* **7**, 106–113 (2001).
15. Wroblewska, L. *et al.* Mammalian synthetic circuits with RNA binding proteins for RNA-only delivery. *Nat. Biotechnol.* **33**, 839–841 (2015).
16. Nakanishi, H. & Saito, H. Caliciviral protein-based artificial translational activator for mammalian gene circuits with RNA-only delivery. *Nat. Commun.* **11**, 1297 (2020).
17. Endo, K., Hayashi, K., Inoue, T. & Saito, H. A versatile cis-acting inverter module for synthetic translational switches. *Nat. Commun.* **4**, 2393 (2013).
18. Raught, B. & Gingras, A. C. eIF4E activity is regulated at multiple levels. *Int. J. Biochem. Cell Biol.* **31**, 43–57 (1999).
19. Kurosaki, T., Popp, M. W. & Maquat, L. E. Quality and quantity control of gene expression by nonsense-mediated mRNA decay. *Nat. Rev. Mol. Cell Biol.* **20**, 406–420 (2019).
20. Stroppel, A. S., Lappalainen, R. & Stafforst, T. Controlling Site-Directed RNA Editing by Chemically Induced Dimerization. *Chem. Eur. J* **27**, 12300–12304 (2021).

21. Rauch, S., Jones, K. A. & Dickinson, B. C. Small Molecule-Inducible RNA-Targeting Systems for Temporal Control of RNA Regulation. *ACS Cent. Sci.* **6**, 1987–1996 (2020).
22. Savva, Y. A., Rieder, L. E. & Reenan, R. A. The ADAR protein family. *Genome Biol.* **13**, 252 (2012).
23. Pollock, R., Giel, M., Linher, K. & Clackson, T. Regulation of endogenous gene expression with a small-molecule dimerizer. *Nat. Biotechnol.* **20**, 729–733 (2002).
24. Pokharel, S. & Beal, P. A. High-throughput screening for functional adenosine to inosine RNA editing systems. *ACS Chem. Biol.* **1**, 761–765 (2006).
25. Katz, N. *et al.* Overcoming the design, build, test bottleneck for synthesis of nonrepetitive protein-RNA cassettes. *Nat. Commun.* **12**, 1576 (2021).
26. Loughran, G., Howard, M. T., Firth, A. E. & Atkins, J. F. Avoidance of reporter assay distortions from fused dual reporters. *RNA* **23**, 1285–1289 (2017).
27. Rodriques, S. G. *et al.* RNA timestamps identify the age of single molecules in RNA sequencing. *Nat. Biotechnol.* **39**, 320–325 (2021).
28. Katrekar, D. *et al.* In vivo RNA editing of point mutations via RNA-guided adenosine deaminases. *Nat. Methods* **16**, 239–242 (2019).
29. Kuttan, A. & Bass, B. L. Mechanistic insights into editing-site specificity of ADARs. *Proc Natl Acad Sci USA* **109**, E3295-304 (2012).
30. Thuy-Boun, A. S. *et al.* Asymmetric dimerization of adenosine deaminase acting on RNA facilitates substrate recognition. *Nucleic Acids Res.* **48**, 7958–7972 (2020).
31. Daringer, N. M., Dudek, R. M., Schwarz, K. A. & Leonard, J. N. Modular extracellular sensor architecture for engineering mammalian cell-based devices. *ACS Synth. Biol.* **3**, 892–902 (2014).
32. Barnea, G. *et al.* The genetic design of signaling cascades to record receptor activation. *Proc Natl Acad Sci USA* **105**, 64–69 (2008).
33. Postiglione, L., Wan, J., di Bernardo, M. & Marucci, L. A strategy for multicellular feedback control in mammalian cells. in *2019 18th European Control Conference (ECC)* 2669–2674 (IEEE, 2019). doi:10.23919/ECC.2019.8796200.
34. Sukumaran, S. *et al.* Enhancing the potency and specificity of engineered T cells for cancer treatment. *Cancer Discov.* **8**, 972–987 (2018).
35. Kipniss, N. H. *et al.* Engineering cell sensing and responses using a GPCR-coupled CRISPR-Cas system. *Nat. Commun.* **8**, 2212 (2017).
36. Wu, B., Chen, J. & Singer, R. H. Background free imaging of single mRNAs in live cells using split fluorescent proteins. *Sci. Rep.* **4**, 3615 (2014).
37. Chen, W., Qin, Y. & Liu, S. CCL20 signaling in the tumor microenvironment. *Adv. Exp. Med. Biol.* **1231**, 53–65 (2020).
38. Ma, Y. *et al.* Synthetic mammalian signaling circuits for robust cell population control. *Cell* **185**, 967-979.e12 (2022).
39. Chung, H. K. & Lin, M. Z. On the cutting edge: protease-based methods for sensing and controlling cell biology. *Nat. Methods* **17**, 885–896 (2020).
40. Iwamoto, M., Björklund, T., Lundberg, C., Kirik, D. & Wandless, T. J. A general chemical method to regulate protein stability in the mammalian central nervous system. *Chem. Biol.* **17**, 981–988 (2010).
41. Chen, Z. & Elowitz, M. B. Programmable protein circuit design. *Cell* **184**, 2284–2301 (2021).

42. Vlahos, A. E. *et al.* Protease-controlled secretion and display of intercellular signals. *Nat. Commun.* **13**, 912 (2022).
43. Tycko, J. *et al.* High-Throughput Discovery and Characterization of Human Transcriptional Effectors. *Cell* **183**, 2020-2035.e16 (2020).
44. Toda, S. *et al.* Engineering synthetic morphogen systems that can program multicellular patterning. *Science* **370**, 327–331 (2020).
45. Hart, Y. *et al.* Paradoxical signaling by a secreted molecule leads to homeostasis of cell levels. *Cell* **158**, 1022–1032 (2014).
46. Cho, K. F. *et al.* A light-gated transcriptional recorder for detecting cell-cell contacts. *eLife* **11**, (2022).
47. Karikó, K. *et al.* Incorporation of pseudouridine into mRNA yields superior nonimmunogenic vector with increased translational capacity and biological stability. *Mol. Ther.* **16**, 1833–1840 (2008).
48. Andries, O. *et al.* N(1)-methylpseudouridine-incorporated mRNA outperforms pseudouridine-incorporated mRNA by providing enhanced protein expression and reduced immunogenicity in mammalian cell lines and mice. *J. Control. Release* **217**, 337–344 (2015).
49. Karijolich, J. & Yu, Y.-T. Converting nonsense codons into sense codons by targeted pseudouridylation. *Nature* **474**, 395–398 (2011).
50. Liu, A. & Wang, X. The Pivotal Role of Chemical Modifications in mRNA Therapeutics. *Front. Cell Dev. Biol.* **10**, 901510 (2022).
51. Warren, L. *et al.* Highly efficient reprogramming to pluripotency and directed differentiation of human cells with synthetic modified mRNA. *Cell Stem Cell* **7**, 618–630 (2010).
52. Edelstein, H. I. *et al.* Elucidation and refinement of synthetic receptor mechanisms. *Synth Biol (Oxf)* **5**, ysaa017 (2020).
53. Yang, Z.-J., Yu, Z.-Y., Cai, Y.-M., Du, R.-R. & Cai, L. Engineering of an enhanced synthetic Notch receptor by reducing ligand-independent activation. *Commun. Biol.* **3**, 116 (2020).
54. Dousis, A., Ravichandran, K., Hobert, E. M., Moore, M. J. & Rabideau, A. E. An engineered T7 RNA polymerase that produces mRNA free of immunostimulatory byproducts. *Nat. Biotechnol.* **41**, 560–568 (2023).
55. Oude Blenke, E. *et al.* The Storage and In-Use Stability of mRNA Vaccines and Therapeutics: Not A Cold Case. *J. Pharm. Sci.* **112**, 386–403 (2023).
56. Leppek, K. *et al.* Combinatorial optimization of mRNA structure, stability, and translation for RNA-based therapeutics. *Nat. Commun.* **13**, 1536 (2022).
57. Chen, R. *et al.* Engineering circular RNA for enhanced protein production. *Nat. Biotechnol.* **41**, 262–272 (2023).
58. Stark, M. R. & Rader, S. D. Efficient splinted ligation of synthetic RNA using RNA ligase. *Methods Mol. Biol.* **1126**, 137–149 (2014).
59. Hernandez-Lopez, R. A. *et al.* T cell circuits that sense antigen density with an ultrasensitive threshold. *Science* **371**, 1166–1171 (2021).
60. Choe, J. H. *et al.* SynNotch-CAR T cells overcome challenges of specificity, heterogeneity, and persistence in treating glioblastoma. *Sci. Transl. Med.* **13**, (2021).
61. Allen, G. M. *et al.* Synthetic cytokine circuits that drive T cells into immune-excluded tumors. *Science* **378**, eaba1624 (2022).

62. Kaseniit, K. E. *et al.* Modular, programmable RNA sensing using ADAR editing in living cells. *Nat. Biotechnol.* **41**, 482–487 (2023).

Acknowledgments

This work was funded by NIH (R00EB027723, R21EB033858, DP2OD034951; XJG), NARSAD Young Investigator Grant from Brain & Behavior Research Foundation (XJG), Longevity Impetus Grants (X.J.G.), Stanford Cancer Institute Innovative Award (XJG), Stanford Interdisciplinary Graduate Fellowship affiliated with ChEM-H (XZ), Stanford Graduate Fellowship in Science & Engineering (LSM), and Stanford University Sarafan ChEM-H CBI Training Program (LSM).

We thank Prof. Lacramioara Bintu for gift of the HEK293 cell line, and Prof. Howard Chang for gift of the Colo 320DM cell line. We thank Prof. Alice Ting for membrane-bound chemokine and their receptor plasmids. We thank Andrew Lu and Prof. Michael Elowitz for the IVT plasmid backbone. We thank Siranush Babakhanova for testing early versions of LIDAR. We thank the Gao lab members for their feedback. We thank Noa Katz for tTA reporter plasmid, and Alex E. Vlahos for plasmid encoding IL-2.

Author Contributions

XZ, LSM, KEK and XJG designed the study. XZ, LSM, KEK, CCC, MZ, YH and XJG developed the methodologies. XZ, LSM, KEK, CCC, MZ and YH performed the experiments. XZ, LSM, CCC, MZ and YH analyzed and processed the data. XZ, LSM and XJG wrote the manuscript with input from all authors.

Competing interests

XZ, LSM, KEK, CCC and XJG are co-inventors on a U.S. provisional patent application no.63/399,400 relating sense-and-response of proteins, peptides and small molecules using ligand-induced dimerization activating RNA editing filed by Stanford University. X.J.G. is a co-founder and serves on the scientific advisory board of Radar Tx. K.E.K. is a co-founder and CSO of Radar Tx.

Materials and Methods

Plasmid generation

Plasmids were generated using standard molecular cloning practices, including InFusion of linearized plasmids and PCR fragments, restriction–ligation of linearized fragments and annealed phosphorylated oligonucleotides. A complete list of plasmids and associated maps can be found in Supplementary Table 1. Plasmids are available upon request from the corresponding author and are deposited to Addgene. Plasmid sources for AVPR2, β-arrestin2 (ARRB2), OXTR, B2AR were acquired from Addgene. Plasmid sources for CCR6, CCR7 as well as their cognate ligands were gifts from Prof. Alice Ting.

Tissue culture

All cell lines were cultured in a humidity-controlled incubator under standard culture conditions (37 °C with 5% CO2). HEK293 cells (catalog no. CRL-1573) and SNU-475 cells (catalog no.

CRL-2236), purchased from ATCC, were cultured using Dulbecco's modified Eagle's medium, supplemented with 10% fetal bovine serum (FBS) (Fisher Scientific catalog no. FB12999102), 1 mM sodium pyruvate (EMD Millipore catalog no. TMS-005-C), 1× penicillin–streptomycin (Genesee catalog no. 25-512), 2 mM L-glutamine (Genesee catalog no. 25-509) and 1× MEM non-essential amino acids (Genesee catalog no. 25-536). C3H mouse fibroblast cells (ATCC catalog no. CCL-226) were cultured according to ATCC's suggested protocol using Eagle's Basal medium (Thermofisher catalog no. 21010-046) supplemented with heat-inactivated FBS to a final concentration of 10%, 1% Penicillin/Streptomycin and 2mM L-glutamine (ATCC 30-2214). Similarly, Colo 320DM cells (gift from Prof. Howard Chang) were cultured according to ATCC's suggested protocol. RPMI medium supplement with 10% FBS and 1% Penicillin/Streptomycin was used to culture these cells.

DNA Transient Transfection

HEK293 cells were cultured in 24-well or 96-well tissue culture-treated plates under standard culture conditions. When cells were 70–90% confluent, the cells were transiently transfected with plasmid constructs using the jetOPTIMUS DNA transfection reagent (Polyplus catalog no. 117-15), as per manufacturer's instructions using 0.375 µl of reagent per 50 µl of jetOPTIMUS buffer for 500 ng total DNA transfections in the 24-well format and 0.13 µl of reagent per 12.5 µl of buffer for 130 ng total DNA in the 96-well format. All transfections are detailed in Supplementary Table 2.

Flow cytometry and data analysis

Cells were harvested by trypsinization and resuspended in flow buffer (HBSS + 2.5 mg/mL bovine serum albumin) approximately 48 h after transfection and 24 h after adding the ligand. After 40-µm straining, cells were analyzed by flow cytometry (Biorad ZE5 Cell Analyzer). Data was processed with the CytoFlow Python package (except for Fig. 3E and Supplementary Fig. 3C; refer to cell surface staining section for specific data analysis method), and cells were gated on the highly transfected populations based on mCherry levels. Unless specifically stated, the 99.5 to 99.9 percentile mCherry (transfection marker) level of the lowest-transfected replicate is used to gate all samples within a comparison set as done in our previous work [62]. In most figures, each plot consists of a comparison set. In a few cases, we use broken x-axes to indicate separate comparison sets within a plot. Unless specifically mentioned, all bars in one single bar plot are gated using the same mCherry fluorescence gate. Values are reported as the means of at least three biological replicates. For experiments comparing two groups, a Bonferroni-corrected two-tailed Student's t-test was used to assess significance. * indicates to $P<0.05$, ** indicates $P< 0.01$, *** indicates $P< 0.001$ and **** indicates $P< 0.0001$.

Cell surface staining

Following 48 hours after DNA transfection, HEK293 cells were pelleted at 300 x g for 7 minutes and reconstituted in PBS supplemented with 5% Bovine Serum Albumin (BSA, company name). Following two wash steps, the cells were incubated with an anti-human IgG antibody conjugated to Alexa Fluor-488 (Southern Biotech Catalog# 2015-30; 1/750 dilution in PBS + 2% BSA) for 1 hour. Following incubation, the cells were washed twice in PBS + 2% BSA and then filtered through a 40 µm sieve. Cells were analyzed by flow cytometry (BioRad ZE5 Cell Analyzer) and Everest Software (version 3.1). FlowJo (version 10.9.0) was used to process the flow cytometry data.

Cell line construction and selection

Polyclonal cell lines were generated using piggyBac stable integration. CCL20-producing cells (XZcp07-membrane and cLSM03-secreted) were each generated using a single transcript containing BFP and puromycin as markers. A double piggyBac integration was done to generate a receiver cell line (cLSM01) containing the entire CCR6-LIDAR circuit. The first construct contained CCR6-ADAR2dd, ARRB2-MCP and Puromycin resistance gene as a selection marker all driven by the EF1-A promoter and separated by IRES and 2A sequences. The second construct contains the LIDAR sensor RNA (mCherry → iCasp9-2A-GFP) driven by SFFV and the hygromycin resistance gene as a selection marker driven by pSV40. Monoclonals were selected by diluting polyclonals to an average of 0.2 cell per well in a 96 well plate. Cells were cultured with selection media using the appropriate antibiotics. Cells were selected based on their capacity to produce GFP and start the apoptotic pathway. The plasmids used to generate all stable cell lines can be found in Supplementary Table 1. Please refer to Supplementary Table 2 for details on transfection.

Co-Culture Experiments

For experiments where cells were transiently transfected, CCL20 sender cells and CCR6-based LIDAR receiver cells were transfected independently. CCL20 sender cells were transfected a day before the CCR6-based LIDAR receiver cells – to allow for the production and secretion of CCL20 into the media – and 24 h after the transfection of the receiver cells, the supernatant of the sender cells was transferred into the receiver cells. The output of the receiver cells was measured using flow cytometry 24h after supernatant transfer. For the membrane-bound CCL20 experiments, sender and receiver cells were transfected separately and then lifted and cultured together 24 h later. The output of the receiver cells was measured using flow cytometry 24 h after co-culture. For experiments using the generated cell lines, cells were cultured together – for both membrane-bound and secreted ligand conditions – and receiver cells were measured after 24 h.

Co-Culture Experiments for Pattern Formation

Custom Polydimethylsiloxane (PDMS, Fisher Scientific #NC9285739) inserts were fabricated using 3D-printed resin molds and 1 (or 2) mm biopsy punches (Fisher Scientific #12-460-402). Printed molds were washed with isopropanol after printing, further cured under UV light for 30 min and placed at 75C for 8h to ensure the reaction had finished. After the mold was fully cured, PDMS was mixed 10:1 (w/w) (base:curing agent), de-gassed, poured into the first mold inside a petri dish and cured at 75C for 1-2 h. Resulting PDMS pieces were further processed using the biopsy punches to make a hole in the center and produce the final PDMS insert. A second mold was used to ensure the punched hole was centered. Final PDMS inserts were sterilized using the autoclave or by placing them under UV light for 30 min inside a petri dish with 70% ethanol. After sterilization, inserts were placed inside a well of a 24 well plate. Monoclonal receiver (cLSM01) and sender (XZcp07 or cLSM03) cells were lifted, spun down, resuspended on fresh media, counted and diluted to 10^6 cells/mL. Sender cells were seeded (5uL of diluted cells) inside the insert and receiver cells on the outside (120 uL of diluted cells). The insert was removed 16-24 h later. Cells were cultured as described above. Images were taken 1-2 days after the insert was removed to allow cells to occupy the empty space (Supplementary Fig. 4A).

Cell Death Assay

Monoclonal cLSM01 cells were seeded in a 24 well plate using 0.5 mL/well of resuspended cells (10^6 cell/mL, final concentration) to ensure all the wells had the same initial confluency. Recombinant CCL20 was added 12 h after seeding and AP1903 was added 24 h after seeding. Refer to Supplementary Table 3 for ligand catalog and concentration used. Images were taken and flow cytometry was performed 12 after adding (36 h after seeding) AP1903. The full process was done within a doubling cycle (36 h) to primarily account for the effect of cell death and eliminate any interference coming from potential differences in growth rates between wells and conditions.

Image acquisition and processing

All images were taken using an EVOS M7000 Cell Imaging System. Co-culture cell patterning images were taken using the automated tile-stitching feature of the imaging system. Co-culture images were processed using ImageJ (FIJI for MacOS) by first subtracting the background for all channels (Process->Subtract background…) using a 100-pixel window ("rolling ball" in ImageJ) and then by linearly enhancing the brightness and contrast of the images to aid with visualization. Composite images were also generated in ImageJ by merging the images of previously processed individual channels (Image->Color->Merge channels). Cell death images were only processed to linearly enhance contrast and brightness. For the images in the first column of Supplementary Fig. 3A, binary masks were generated by segmenting (i.e., thresholding and binarization) the dead cells in the bright field images. Segmentation was done based on morphological differences between healthy and dead cells, i.e., the difference in brightness and roundness of dead cells compared to live cells. Final cell death images were generated by overlaying bright field images with the masks corresponding to death cells. For both co-culture and cell death figures, each channel was processed independently.

Pattern Formation experiments quantification and plotting.

Previously processed green channel images were analyzed using a MATLAB script. Average intensities were calculated from the center of the circular patterns outwards (Supplementary Fig. 4D) and then these values were normalized to account for different background and intensity values in each individual image. Given that the different circular patterns obtained had slightly different diameters due to cell growth, the data was further processed to align global maximas corresponding to the interface between the two populations of cells. A low-pass filter was also applied to the data by using a 3-value moving average. The final plots are shown in Fig. 4E. The codes used to process this data can be found in the supplementary materials.

mRNA synthesis and transfection

The DNA templates for in vitro transcription were prepared by PCR on a plasmid template containing the LIDAR coding sequences flanked by optimal 5' and 3' UTRs as well as a T7 promoter. The plasmid template with optimal UTRs was a gift from Prof. Michael Elowitz. Poly-A tail was added to the DNA template by PCR with reverse primer containing a 200bp polyA sequence. In vitro transcribed mRNA was produced and purified by GeneScript Inc. based on the DNA template, with Cap1 capping and optional base modifications. The purified mRNAs were then transfected to specific HEK cell lines as needed by Mirus TransIT®-mRNA Transfection Kit following the manufacturer's instructions. In addition, cells were transfected when they reached >90% confluency, 3 µl of TransIT-mRNA reagent as well as mRNA boost was used per

well in 24 well plate, and the ligand was supplied together with mRNA transfection. Expression of fluorescent proteins on the mRNA was assayed through flow cytometry 24 hours post mRNA transfection.

Data Availability

Plasmid maps can also be found in Supplementary Table 1. Raw data, as well as the code used for its analysis, is available upon request from the corresponding author.

Supplementary Materials

Supplementary Figure 1
Supplementary Figure 2
Supplementary Figure 3
Supplementary Figure 4
Supplementary Figure 5
Supplementary Table 1. List of plasmids (LIDAR)
Supplementary Table 2. Overview of transfections
Supplementary Table 3. List of ligands